DYNAMICS OF FLEXIBLE FILAMENTS IN VISCOUS FLUIDS

CASPER H. L. BEENTJES

Mathematical Institute, University of Oxford, Oxford, UK

Abstract. Inspired by the locomotion of organisms at the micro-scale using appendages we derive a simplified model of a flagellum-like micro-swimmer. Based on the work by [2, 19] we study a passive one-dimensional elastic filament immersed in a viscous fluid driven by an external torque on the head of the filament. We derive an elastohydrodynamic model describing the fluid-filament interaction. Using weakly non-linear analysis and numerical simulations we show that this simple model indeed can describe the propulsion of a filament. The model gives a non-zero and non-trivial swimming speed which depends only on two non-dimensional model-parameters, viscous drag anisotropy and a filament property parameter.

1. Introduction

Since the development of the microscope roughly 4 centuries ago a whole new world of organisms came into view, the world of micro-scale organisms. It turns out that even on this scale there is room for complex dynamics. The movement of micro-organisms, such as bacteria moving to regions of higher nutrient concentration or spermatozoa trying to reach the ovum, turns out to be far from being trivial. The world of these micro-swimmers and the way they cruise through their environment does not bear any resemblance to our world, with striking examples such as the corkscrew-like rotating filament which helps to propel the *E. coli* bacterium.

If dolphins can swim effectively in a rough ocean, why does it seem that bacteria had to come up with completely different tactics to move through a fluid? Is there a difference between macro-swimmers and micro-swimmers, and if so why?

This paper first motivates the difference in scale and the effects it has on locomotion. Subsequently, we derive a model for the propulsion of a simplified micro-organism, an (elastic) filament in a viscous fluid. The resulting model is then analysed using both numerical and (semi-)analytical techniques which show that this model, although simple in nature, can indeed describe a moving filament.

1.1. Life at low Reynolds number.

In order to distinguish our macro-world from the micro-scale, we recall that we are interested in motion in fluid-like environments. The natural framework for these kind of problems is the field of hydrodynamics. To study the motion of incompressible viscous fluids one often uses the incompressible Newtonion Navier-Stokes equations[1]. These

E-mail address: beentjes@maths.ox.ac.uk.

Date: Hilary term 2015.

2010 *Mathematics Subject Classification.* 74F10, 76Z10, 74S25.

This text is based on a technical report for the Modelling Case Study during Hilary 2015 for the Oxford Mathematics MSc. in Mathematical Modelling & Scientific Computing.

[1]Note that suitable boundary conditions have to be chosen depending on the problem considered in order to be able to find a solution. Here we omit details about boundary conditions as they are not of direct interest at this point.

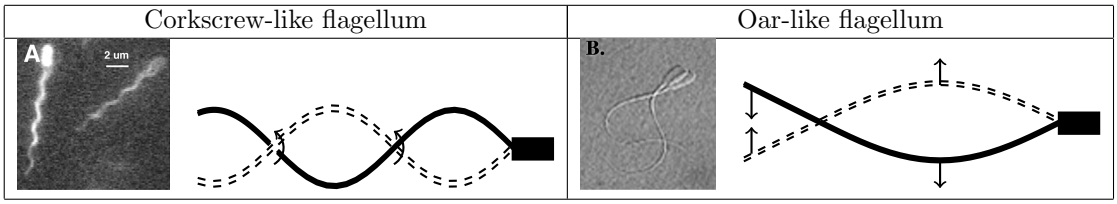

FIGURE 1. *Left*: Fluorescently labelled *E. Coli* bacteria using corkscrew-like flagella, image by [3]. *Right*: Stroboscopic image of a (bovine) spermatozoa using an oar-like flagellum, image by [12].

equations can be cast in non-dimensional form

$$Re\left[\frac{\partial}{\partial t}+\mathbf{u}\cdot\nabla\right]\mathbf{u}=-\nabla p+\nabla^2\mathbf{u},\qquad \nabla\cdot\mathbf{u}=0, \tag{1}$$

where $\mathbf{u}$ is the velocity field, p the pressure and Re the Reynolds number, given by

$$Re=\frac{\rho UL}{\mu}. \tag{2}$$

Here μ is the dynamic viscosity, ρ the density of the fluid and U, L typical velocity and length scales of the problem respectively.

This number can be seen as a ratio of inertial forces, characterised by ρU^2L^2, over the viscous forces, characterised by μUL. This number provides crucial insight into the difference between our world and that of bacteria. Since for the micro-organisms the typical length and velocity scale are very small, we are in the realm of low Reynolds numbers ranging from $Re\sim 10^{-5}$ to 10^{-2} [10]. This in contrast to swimming dolphins in water for which the Reynolds number is several orders of magnitude bigger, $Re\sim 10^6$ [15]. As a result, the motion of micro-organisms is dictated by viscous forces and the influence of inertia is negligible, contrasting the inertia dominated movement by macro-scale animals. This was observed in classical works by Taylor [16] and Purcell [13].

Looking at (1) for low Reynolds numbers, i.e. $Re\ll 1$, we see that we can neglect inertial contributions and arrive at the Stokes equations,

$$\mathbf{0}=-\nabla\hat{p}+\nabla^2\hat{\mathbf{u}},\qquad \nabla\cdot\hat{\mathbf{u}}=0. \tag{3}$$

One striking feature of this set of equations is that the equations are time-independent, time now merely serves as a parameter instead of a variable. In addition, the system is linear in its variables. Combining these results we can state the so-called *Scallop Theorem* first formulated in 1977 by Purcell [13]; at low Reynolds numbers no net movement can be achieved by reciprocal movement, i.e. movement which is invariant under time-reversal. This follows from the fact that the displacement by the forward part of the movement cancels with the backward part of the movement, regardless of the time it takes for both parts as the equations (3) are time-independent. This statement allows us now to explain why micro-swimmers have to use a different strategy. Almost all swimming motion at the macro-scale is time-reversible and therefore, although effective at high Reynolds numbers, unable to generate net propulsion at the micro-scale. Purcell stated two different ways, inspired by observations in nature, to overcome this barrier. The first one, which is nowadays more widely studied, is the use of a corkscrew-like flagellum. The other method uses a flexible filament which is used as an oar to elude The Scallop Theorem, see Figure 1 for examples of both methods. It is the latter idea which forms the basis of the model in this paper, inspired by the work of Wiggins et al. [19, 20] and Camalet et al. [2].

2. Model

A considerable group of micro-organisms makes use of flexible appendages as oars to generate movement [10]. Spermatozoa of several species are a notable example (see Figure 1), they use propagation of waves along their tail to induce propulsion. These form a major inspiration for the work carried out by Wiggins et al. [20], who analysed one-dimensional elastic filaments in a viscous fluid. This approach combines viscous effects using hydrodynamics and flexibility of the filament by elastics to derive an elastohydrodynamic model describing the movement of the filament.

This paper takes a similar route by considering a passive one-dimensional filament of length L. Its movement is constrained to the plane to keep analysis tractable. Moreover, as Wiggins et al. noted, this is one of the most suitable geometries to acquire experimental data.

The geometry of the filament can be described by considering a parametrisation in terms of the arclength s. A natural parametrisation of the filament position $\mathbf{r}(s)$ is given by the angle $\psi(s)$ that the local tangent vector $\hat{\mathbf{t}}(s)$ makes with the horizontal axis, see Figure 2. This yields the parametrisation

$$\mathbf{r}(s) = \mathbf{r}(0) + \int_0^s \hat{\mathbf{t}}(s')\,\mathrm{d}s' = \mathbf{r}(0) + \int_0^s \begin{pmatrix}\cos\psi(s')\\ \sin\psi(s')\end{pmatrix}\,\mathrm{d}s'. \tag{4}$$

To derive an equation for the change of the shape $\mathbf{r}(s,t)$ due to dynamic effects, let us recall the result of low Reynolds numbers, namely negligible inertia. Combining this with the lack of active elements along the filament the local force-balance on the filament simplifies to

$$\mathbf{f}_{\mathcal{H}} + \mathbf{f}_{\mathcal{E}} = \mathbf{0}, \tag{5}$$

where $\mathbf{f}_{\mathcal{H}}, \mathbf{f}_{\mathcal{E}}$ denote the hydrodynamic force and elastic force on the filament respectively. Deriving the model then in essence boils down to modelling these two forces.

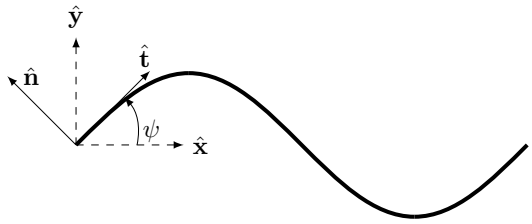

Figure 2. Geometry of the one-dimensional filament. The angle $\psi(s)$ of the local tangent $\hat{\mathbf{t}}(s)$ with the horizontal coordinate axis allows a natural parametrisation of the curve. Here s depicts the arclength parameter. Note that $\mathbf{r}_s = \hat{\mathbf{t}}$.

2.1. Hydrodynamic force.

In the Stokes regime for flow the drag velocity can be shown to be a linear function of the velocity $\mathbf{u}$, with the most common known example the Stokes law for drag on a sphere in a viscous fluid. However, if the geometry is not as simple as a sphere the derivation becomes much more cumbersome. The Stokes paradox even prohibits a non-trivial flow-solution around an infinitely long cylinder [4]. To derive a relation between force and velocity for a finite length cylinder, which would describe our filament, we follow the approach set out initially by Hancock [7]. The general idea, as described by Lighthill [11] and usually called slender-body theory, is to use linearity of the Stokes equations. One can hope to build a solution by using superposition of point sources, i.e. solutions to

$$-\mathbf{F}\delta(\mathbf{r}) = -\nabla p + \nabla^2\mathbf{u}, \qquad \nabla\cdot\mathbf{u} = 0. \tag{6}$$

By combining monopole and dipole point sources, ced Stokeslet and source-doublet respectively, one can construct a solution on a finite length cylinder (see appendix A.2 for more details). The resulting relation between drag and velocity can be written as

$$\mathbf{f}_{\mathcal{H}} = -\xi_{\parallel}\mathbf{u}_{\parallel} - \xi_{\perp}\mathbf{u}_{\perp}. \tag{7}$$

The drag can be decomposed in components tangential and perpendicular to the filament, both linearly dependent on the local velocity components in that direction. From the slender-body theory follows that in the limit of very slender filaments

$$\xi_{\perp} = 2\xi_{\parallel}, \tag{8}$$

giving anisotropy in the drag. The drag in the perpendicular direction is twice the size of that parallel to the filament. It turns out that this anisotropy is crucial in the process of propelling the filament as it creates a propulsive force perpendicular to the local velocity, see Figure 3. If we can combine anisotropy with a time-irreversible motion of the filament, we can create propulsion of the filament. We rewrite the hydrodynamic force to a form which envisions the effect of the anisotropy clearer,

$$\mathbf{f}_{\mathcal{H}} = -\xi_{\perp}[\hat{\mathbf{n}}\hat{\mathbf{n}} + \beta\hat{\mathbf{t}}\hat{\mathbf{t}}] \cdot \mathbf{u}, \tag{9}$$

where now $\beta = \frac{\xi_{\parallel}}{\xi_{\perp}}$ tunes the anisotropy. Note that $\beta = 1$ recovers perfect isotropy and slender-body theory predicts $\beta = \frac{1}{2}$ for very slender filaments, which therefore is the value chosen in the rest of this paper unless stated otherwise.

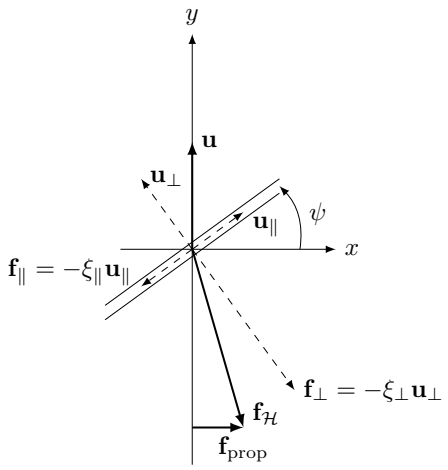

FIGURE 3. The local drag can be decomposed into its perpendicular and parallel component, which are both opposite in direction to the velocity components. By anisotropy of the viscous drag a propulsive force $\mathbf{f}_{\text{prop}}$ perpendicular to the local velocity $\mathbf{u}$ can be generated.

2.2. **Elastic force.** In order to derive the elastic force on the filament we follow a variational approach, set out by Camalet et al. [2]. Flexing of the filament induces a change in geometry, which we describe using the local angle $\psi(s)$, see Figure 2. From this local angle we can infer the curvature κ of the filament as $\kappa = \psi_s$. Using κ we can write down the bending energy of a filament,

$$E_{elastic} = \frac{1}{2}EI\int_0^L \kappa^2 \,\mathrm{d}s = \frac{1}{2}A\int_0^L \kappa^2 \,\mathrm{d}s. \tag{10}$$

Here E, I are the Young's modulus and area moment of inertia respectively, material and geometrical parameters, which we lump together in the bending-stiffness parameter A.
If we then use an inextensible filament we need to impose a constraint of conserved arclength, i.e. locally $|\mathbf{r}_s|^2 = 1$. This is achieved by adding a Lagrange multiplier Λ to the energy,

$$E_{elastic} = \frac{1}{2}\int_0^L A\kappa^2 + \Lambda|\mathbf{r}_s|^2 \,\mathrm{d}s. \tag{11}$$

By considering variations on the shape of the filament, $\delta\mathbf{r}$, we arrive at a variation of the energy $\delta E_{elastic}$ (see appendix A.1 for details),

$$\begin{aligned}\delta E_{elastic} &= \left[A\kappa\hat{\mathbf{n}}\cdot\delta\mathbf{r}_s + \left(-A\kappa_s\hat{\mathbf{n}} + \tau\hat{\mathbf{t}}\right)\cdot\delta\mathbf{r}\right]_0^L + \int_0^L \partial_s[A\kappa_s\hat{\mathbf{n}} - \tau\hat{\mathbf{t}}]\cdot\delta\mathbf{r}\,\mathrm{d}s \\ &= [\mathbf{M}_{ext}\cdot\delta\mathbf{r}_s + \mathbf{F}_{ext}\cdot\delta\mathbf{r}]_0^L + \int_0^L \frac{\delta E_{elastic}}{\delta\mathbf{r}}\cdot\delta\mathbf{r}\,\mathrm{d}s,\end{aligned} \tag{12}$$

where we have introduced the tension $\tau = A\kappa^2 + \Lambda$. The boundary terms contain contributions of any externally applied forces $\mathbf{F}_{ext}$ or torques $\mathbf{M}_{ext}$ at the ends of the filament and these will result in boundary conditions for the model. This will be specified in subsequent sections as it depends on the specific setting of the problem. For now it is important to note that the elastic force follows from taking the functional derivative of the energy,

$$\mathbf{f}_{\mathcal{E}} = -\frac{\delta E_{elastic}}{\delta\mathbf{r}} = -\partial_s[A\kappa_s\hat{\mathbf{n}} - \tau\hat{\mathbf{t}}]. \tag{13}$$

Now we expand the derivatives and use the Frenet-Serret relations,

$$\hat{\mathbf{n}}_s = -\kappa\hat{\mathbf{t}}, \qquad \hat{\mathbf{t}}_s = \kappa\hat{\mathbf{n}}, \tag{14}$$

to rewrite the force in a more useful format for later analysis

$$\mathbf{f}_{\mathcal{E}} = -(A\psi_{sss} - \psi_s\tau)\hat{\mathbf{n}} + (A\psi_{ss}\psi_s + \tau_s)\hat{\mathbf{t}}. \tag{15}$$

2.3. **Force balance equation.** All the ingredients are now ready to derive the model equation for the elastic filament in a viscous fluid. Using (5) and the derived expressions for the forces we find the governing dynamic equation,

$$-\xi_\perp[\hat{\mathbf{n}}\hat{\mathbf{n}} + \beta\hat{\mathbf{t}}\hat{\mathbf{t}}]\cdot\mathbf{u} = (A\psi_{sss} - \psi_s\tau)\hat{\mathbf{n}} - (A\psi_{ss}\psi_s + \tau_s)\hat{\mathbf{t}}. \tag{16}$$

Now we can rewrite this to a more appealing form containing just the velocity $\mathbf{u}$ on the left-hand side

$$\mathbf{u} = \frac{1}{\xi_\perp}(-A\psi_{sss} + \psi_s\tau)\hat{\mathbf{n}} + \frac{1}{\beta\xi_\perp}(A\psi_{ss}\psi_s + \tau_s)\hat{\mathbf{t}}. \tag{17}$$

Non-dimensionalisation. To carry out more detailed analysis on this equation we carry out a non-dimensionalisation using

$$s = L\hat{s}, \qquad t = T\hat{t}, \qquad \tau = \frac{A}{L^2}\hat{\tau}, \qquad \psi = \hat{\psi}, \tag{18}$$

where T is a typical time-scale which can be freely chosen. Upon dropping the hats we get a non-dimensional equation containing two parameters

$$\mathrm{Sp}^4\mathbf{u} = (-\psi_{sss} + \psi_s\tau)\hat{\mathbf{n}} + \frac{1}{\beta}(\psi_{ss}\psi_s + \tau_s)\hat{\mathbf{t}}, \tag{19}$$

the sperm-number Sp [5] and drag-ratio β

$$\mathrm{Sp} = L\left(\frac{\xi_\perp}{AT}\right)^{\frac{1}{4}}, \qquad \beta = \frac{\xi_\parallel}{\xi_\perp}. \tag{20}$$

This is a vectorial equation and it can be split in two components using

$$\mathbf{u}_s = (\mathbf{r}_t)_s = (\mathbf{r}_s)_t = \hat{\mathbf{t}}_t = \psi_t \hat{\mathbf{n}}. \tag{21}$$

The result is a non-linear (high-order) coupled PDE-ODE system for ψ, τ,

$$\begin{cases} \mathrm{Sp}^4 \psi_t &= -\psi_{ssss} + (1+\frac{1}{\beta})\psi_s \tau_s + \psi_{ss}(\tau + \frac{1}{\beta}\psi_s^2), \\ \tau_{ss} &= \beta \psi_s^2 \tau - \psi_{ss}^2 - (1+\beta)\psi_s \psi_{sss}. \end{cases} \tag{22}$$

In order for the problem to be well-posed we need to prescribe boundary conditions (and initial conditions), which depends on the setup of the model.

2.4. **Propelled movement.** In order to make the passive filament move we have to invoke dynamics on the filament externally. The choice made for this paper is to prescribe the angle $\psi(0,t)$, i.e. the angle of the head of the filament. In practise this can be realised by application of an external torque $\mathbf{M}_{ext}$ at the head. It is most practical to drive the angle in a periodic fashion, with frequency ω. This yields a natural time scale T for the problem, namely $T = \frac{2\pi}{\omega}$ and thus $\mathrm{Sp} = L\left(\frac{\omega \xi_\perp}{2\pi A}\right)^{\frac{1}{4}}$. The value for Sp for human-spermatozoa is estimated to lie in the range between 4 and 24 [5].

The rest of the boundary conditions have to follow from the boundary terms in (12), giving the natural boundary conditions. The tail of the filament is let free and thus experiences no external torque,

$$\mathbf{0} = \mathbf{M}_{ext} = \kappa \hat{\mathbf{n}} = \psi_s \hat{\mathbf{n}} \qquad \text{at } s = 1. \tag{23}$$

No force is applied at both ends and this yields

$$\mathbf{0} = \mathbf{F}_{ext} = -\kappa_s \hat{\mathbf{n}} + \tau \hat{\mathbf{t}} = -\psi_{ss} \hat{\mathbf{n}} + \tau \hat{\mathbf{t}} \qquad \text{at } s = 0, s = 1. \tag{24}$$

Upon splitting the boundary conditions into components we derive the complete set of boundary conditions for the driven filament problem

$$\begin{cases} \psi = f(t), \quad \psi_{ss} = 0, \quad \tau = 0 & s = 0, t \geq 0, \\ \psi_s = 0, \quad \psi_{ss} = 0, \quad \tau = 0 & s = 1, t \geq 0. \end{cases} \tag{25}$$

Together with (22) and initial conditions, such as a filament initially at rest, this constitutes the full main model of this paper.

As we are interested in the propulsion of the filament it is useful to look for a quantity measuring the locomotion. In order to do so we define the average filament velocity, taken to be an average over the period at which we drive the head

$$\mathbf{V} = \int_0^1 \mathbf{u}(t)\,\mathrm{d}t = \mathrm{Sp}^{-4} \int_0^1 (-\psi_{sss} + \psi_s \tau)\hat{\mathbf{n}} + \frac{1}{\beta}(\psi_{ss}\psi_s + \tau_s)\hat{\mathbf{t}}\,\mathrm{d}t, \tag{26}$$

where we use the fact that the period is 1 in the non-dimensional system.

3. Weakly non-linear analysis

As the full model that we have derived is a non-linear PDE system of high-order, it is not expected that analytical progress can be made. Instead we start out with a weakly non-linear analysis, by assuming a small angle expansion. As there is for the general problem no natural small parameter, we can motivate this study by assuming that we drive the angle at the head by a small amplitude,

$$\psi(0,t) = \varepsilon f(t), \qquad \varepsilon \ll 1, \quad |f(t)| = \mathcal{O}(1). \tag{27}$$

Given this small parameter ε we expand the dynamics of the problem in this amplitude

$$\mathbf{u} = \mathbf{u}^{(0)} + \epsilon\mathbf{u}^{(1)} + \epsilon^2\mathbf{u}^{(2)} + \mathcal{O}(\epsilon^3), \tag{28}$$

$$\hat{\mathbf{n}} = \hat{\mathbf{n}}^{(0)} + \epsilon\hat{\mathbf{n}}^{(1)} + \epsilon^2\hat{\mathbf{n}}^{(2)} + \mathcal{O}(\epsilon^3), \tag{29}$$

$$\hat{\mathbf{t}} = \hat{\mathbf{t}}^{(0)} + \epsilon\hat{\mathbf{t}}^{(1)} + \epsilon^2\hat{\mathbf{t}}^{(2)} + \mathcal{O}(\epsilon^3), \tag{30}$$

$$\psi = \psi^{(0)} + \epsilon\psi^{(1)} + \epsilon^2\psi^{(2)} + \mathcal{O}(\epsilon^3), \tag{31}$$

$$\tau = \tau^{(0)} + \epsilon\tau^{(1)} + \epsilon^2\tau^{(2)} + \mathcal{O}(\epsilon^3), \tag{32}$$

and collect terms of equal order upon substitution in the system of equations. The boundary conditions for the problem change to become

$$\forall i \neq 1 \quad \begin{cases} \psi^{(i)} = 0, \quad \psi^{(i)}_{ss} = 0, \quad \tau^{(i)} = 0 & s = 0, t \geq 0, \\ \psi^{(i)}_{s} = 0, \quad \psi^{(i)}_{ss} = 0, \quad \tau^{(i)} = 0 & s = 1, t \geq 0, \end{cases} \tag{33}$$

$$i = 1 \quad \begin{cases} \psi^{(1)} = f(t), \quad \psi^{(1)}_{ss} = 0, \quad \tau^{(1)} = 0 & s = 0, t \geq 0, \\ \psi^{(1)}_{s} = 0, \quad \psi^{(1)}_{ss} = 0, \quad \tau^{(1)} = 0 & s = 1, t \geq 0. \end{cases} \tag{34}$$

As we expand $\mathbf{u}$ in terms of ε it follows that the average velocity can be expanded in the same way

$$\mathbf{V} = \mathbf{V}^{(0)} + \epsilon\mathbf{V}^{(1)} + \epsilon^2\mathbf{V}^{(2)} + \mathcal{O}(\epsilon^3). \tag{35}$$

Trivial order, $\mathcal{O}(1)$. At $\mathcal{O}(1)$ we note that the boundary conditions are homogeneous and the trivial solution $\psi^{(0)} = \tau^{(0)} = 0$ satisfies both the boundary conditions and (22). This makes sense as this describes an initially straight filament, which is the base state around which we start an oscillation by driving it. As a result we find that

$$\hat{\mathbf{n}} = \begin{pmatrix} 0 \\ 1 \end{pmatrix} - \epsilon \begin{pmatrix} \psi^{(1)} \\ 0 \end{pmatrix} - \epsilon^2 \begin{pmatrix} \psi^{(2)} \\ \frac{1}{2}(\psi^{(1)})^2 \end{pmatrix} + \mathcal{O}(\epsilon^3) \quad = \hat{\mathbf{y}} - \varepsilon\psi^{(1)}\hat{\mathbf{x}} - \epsilon^2 \begin{pmatrix} \psi^{(2)} \\ \frac{1}{2}(\psi^{(1)})^2 \end{pmatrix} + \mathcal{O}(\epsilon^3), \tag{36}$$

$$\hat{\mathbf{t}} = \begin{pmatrix} 1 \\ 0 \end{pmatrix} + \epsilon \begin{pmatrix} 0 \\ \psi^{(1)} \end{pmatrix} - \epsilon^2 \begin{pmatrix} \frac{1}{2}(\psi^{(1)})^2 \\ -\psi^{(2)} \end{pmatrix} + \mathcal{O}(\epsilon^3) \quad = \hat{\mathbf{x}} + \varepsilon\psi^{(1)}\hat{\mathbf{y}} - \epsilon^2 \begin{pmatrix} \frac{1}{2}(\psi^{(1)})^2 \\ -\psi^{(2)} \end{pmatrix} + \mathcal{O}(\epsilon^3), \tag{37}$$

so that we can express the local vectors in terms of the coordinate axis $\hat{\mathbf{x}}, \hat{\mathbf{y}}$. These imply the rather trivial result $\mathbf{u}^{(0)} = \mathbf{0}$ and thus $\mathbf{V}^{(0)} = \mathbf{0}$, there is no net propulsion from a straight filament.

Linearised problem, $\mathcal{O}(\varepsilon)$. Using the results from $\mathcal{O}(1)$ we can distil from (22) the $\mathcal{O}(\varepsilon)$ equations

$$\begin{cases} \mathrm{Sp}^4\psi^{(1)}_t & = -\psi^{(1)}_{ssss}, \\ \tau^{(1)}_{ss} & = 0, \end{cases} \tag{38}$$

subject to (34). Note that the equation for $\tau^{(1)}$ readily gives $\tau^{(1)} \equiv 0$, so there is no tension at first order. If we now glance at the expansion for $\mathbf{u}$ we see that

$$\mathrm{Sp}^4\mathbf{u}^{(1)} = -\psi^{(1)}_{sss}\hat{\mathbf{y}} + \frac{1}{\beta}\tau^{(1)}_s\hat{\mathbf{x}} = -\psi^{(1)}_{sss}\hat{\mathbf{y}} \tag{39}$$

and thus there is no velocity in the $\hat{\mathbf{x}}$ direction because of the lack of tension. In order to find a swimming speed we thus need to go to higher orders as $\mathbf{V}^{(1)}$ won't have a component in the direction at which we expect to propel the filament.

However, we still need to look at the equation for $\psi^{(1)}$. One can see that it is a linear PDE and it is in fact a hyperdiffusion equation. This is the same result as found by Wiggins et al. [19], although they worked in the framework of small amplitude deviations in position instead of angle, the latter being a more general framework.

The equation can be solved analytically using the same tools used to solve a diffusion equation. If we assume that we drive the head periodically by a function of the form $f(t) = \mathcal{R}\{e^{i\omega t}\}$, the resulting long-term behaviour, i.e. after the transient problem has died out, is given by a superposition of four travelling waves (compare with two waves in the case of normal Stokes flow cf. [19]). The result, found by separation of variables, is given by

$$\begin{aligned}\psi^{(1)}(s,t) = a_1 e^{\eta\gamma s}\cos(-\eta\sigma s + 2\pi t + \phi_1) + a_2 e^{\eta\sigma s}\cos(\eta\gamma s + 2\pi t + \phi_2) + \dots \\ a_3 e^{-\eta\gamma s}\cos(\eta\sigma s + 2\pi t + \phi_3) + a_4 e^{-\eta\sigma s}\cos(-\eta\gamma s + 2\pi t + \phi_4),\end{aligned} \tag{40}$$

where $\eta = 2\pi\mathrm{Sp}$, $\gamma = \cos\frac{\pi}{8}$, $\sigma = \sin\frac{\pi}{8}$ and $a_i, \phi_i \in \mathbb{R}$ are constants determined by the boundary conditions. Note that we have two travelling waves moving from head to tail and two in the opposite direction. Furthermore one can see that the waves are either exponentially decaying or growing along their direction of propagation.

Taking a derivative with respect to s will not change the dependency on time. Thus taking a time-average over one period of $\psi^{(1)}$ or any of its s-derivatives will inherently give zero result. Going back to (39) and the definition of $\mathbf{V}$ (26) we find that $\mathbf{V}^{(1)} \equiv \mathbf{0}$ and thus at first order the average speed vanishes in all directions.

Weakly non-linear swimming speed, $\mathcal{O}(\varepsilon^2)$. To find a non-vanishing swimming speed we need to consider the quadratic contributions. Using the result that $\tau^{(1)} \equiv 0$ the equations at $\mathcal{O}(\varepsilon^2)$ become

$$\begin{cases} \mathrm{Sp}^4\psi_t^{(2)} &= -\psi_{ssss}^{(2)}, \\ \tau_{ss}^{(2)} &= -(\psi_{ss}^{(1)})^2 - (1+\beta)\psi_s^{(1)}\psi_{sss}^{(1)}. \end{cases} \tag{41}$$

We see that the equation for $\psi^{(2)}$ equals that for $\psi^{(1)}$. Note, however, that the boundary conditions for $\psi^{(2)}$ are homogeneous whereas those for $\psi^{(1)}$ were inhomogeneous. The result of this is that we find that $\psi^{(2)} \equiv 0$. For the tension we see that it does not vanish at second order as we can solve for $\tau^{(2)}$ by integrating twice with respect to s the right hand side of (41) which is completely known by (40). This completely determines the quadratic order, nonetheless it remains tedious work to find the explicit expressions. Continuing along these lines one can show that the expansions of ψ, τ take the form

$$\psi = \epsilon\psi^{(1)} + \epsilon^3\psi^{(3)} + \mathcal{O}(\epsilon^5), \tag{42}$$

$$\tau = \epsilon^2\tau^{(2)} + \epsilon^4\tau^{(4)} + \mathcal{O}(\epsilon^6). \tag{43}$$

Now using (17) we find

$$\begin{aligned}\mathbf{u}^{(2)} &= \frac{1}{\beta}(\psi_s^{(1)}\psi_{ss}^{(1)} + \tau_s^{(2)})\hat{\mathbf{t}}^{(0)} - \psi_{sss}^{(1)}\hat{\mathbf{n}}^{(1)} \\ &= \left(\frac{1}{\beta}(\psi_s^{(1)}\psi_{ss}^{(1)} + \tau_s^{(2)}) + \psi_{sss}^{(1)}\psi^{(1)}\right)\hat{\mathbf{x}},\end{aligned} \tag{44}$$

which gives that

$$\mathbf{V}^{(2)} = \mathrm{Sp}^{-4}\int_0^1 \frac{1}{\beta}(\psi_s^{(1)}\psi_{ss}^{(1)} + \tau_s^{(2)}) + \psi_{sss}^{(1)}\psi^{(1)}\,\mathrm{d}t\;\hat{\mathbf{x}}. \tag{45}$$

We thus find indeed a non-trivial swimming-speed in the $\hat{\mathbf{x}}$ direction at the second order. As the explicit computation of this expression is very cumbersome we omit the details here and will only compare the results with the numerical analysis from the next section.

4. Numerical solution

In order to derive results in the case where $|\psi(0,t)| \sim \mathcal{O}(1)$, we cannot use the weakly non-linear approach any more and because of the intricate nature of the equations we use numerics to compute the solution. We solve the ODE-PDE coupled system (22) for ψ, τ and use (4) to convert this back into the position $\mathbf{r}(s,t)$. Note that we need $\mathbf{r}(0,t)$ in order to compute the shape, i.e. the position of the head. This is encoded in (17) if we note that $\mathbf{u}(0,t) = \partial_t \mathbf{r}(0,t)$. Therefore we can use this to find the change of $\mathbf{r}(0,t)$ in time by evaluating (17) at $s = 0$.

Numerical scheme. To solve (22) numerically we use the method of lines, discretising in space first. A spectral collocation method using a Chebyshev grid [18] was used for spatial discretisation. The result is a system of ODEs for the spatial discretisation $\mathbf{\Psi}$ of ψ and algebraic equations for the spatial discretisation $\mathbf{T}$ of τ. We then step in time using equispaced timesteps Δt. Care must be taken by considering stability of integration as (hyper)diffusion makes the problem stiff, manifested by severe constraints on the stepsize. In order to elude this constraint we use a second order IMEX-method known as IMEX-2BDF or IMEX-SBDF[1, 8] to solve for $\mathbf{\Psi}$ and solve $\mathbf{T}$ at every timestep from the algebraic equations (see A.3 for more detail).

As a driving function for the head we choose

$$f(t) = F\cos(2\pi t), \tag{46}$$

where we can set the amplitude F (results for $F \ll 1$ should agree with Section 3).

We neglect the transient problem by first evolving the filament from the calculated first order approximation (see Section 3) a number of periods to let the transient contribution decay to zero.

4.1. **Results.**

Filament shape. We are able to compute the resulting filament shape for a wide range of values of Sp and F, some resulting filament shapes are depicted in Figure 4. In order to compare the effects on the shape of increasing Sp and a difference in F we have plotted the filament shape in the reference frame which leaves the head of the filament at rest, though note that in the lab frame the filament head describes a non-trivial trajectory through space.

What we can immediately note is that there is qualitatively difference in filament shape as we increase Sp. For very small values of Sp we see that the filament remains straight, i.e. no bending takes place. This follows from the fact that if Sp becomes small the bending forces start to dominate, either because the filament is short or stiff, because the fluid-viscosity is low, or because the driving frequency is low. The result is that the filament will not bend and remains straight, it functions as a stiff oar in a reciprocal movement. Recall then the Scallop theorem, there cannot be any net-propulsion under this circumstances, therefore we should see no net-velocity in this case.

By increasing Sp we start to initiate travelling waves along the filament, like one would expect from the analysis in Section 3. From the linearised problem we saw that Sp can be interpreted as a decay length of the waves, see (40). As a result we note that for larger Sp the waves tend to decay faster towards the end of the filament. We thus expect that in the limit of Sp becoming large that there cannot be any propulsion either, because in that limit the part of the filament that can generate propulsion vanishes whereas the drag-forces increase by definition of Sp. We thus expect to see an optimal point between the limits of small and large Sp in terms of propulsion.

We also compare the (nearly) linear results, i.e. small angle given by a small driving amplitude $F = 0.1$, with the fully non-linear results, with a driving amplitude $F = 1.5$. We can see the main difference, namely a huge difference in amplitude of the filament in the vertical direction, initiated by a bigger driving torque at the head. Another feature we can observe is that there seems to be a gradual way in going from the linear to the non-linear deformed shapes. The qualitative shape does not change much for these values of F. Note however that if we were to

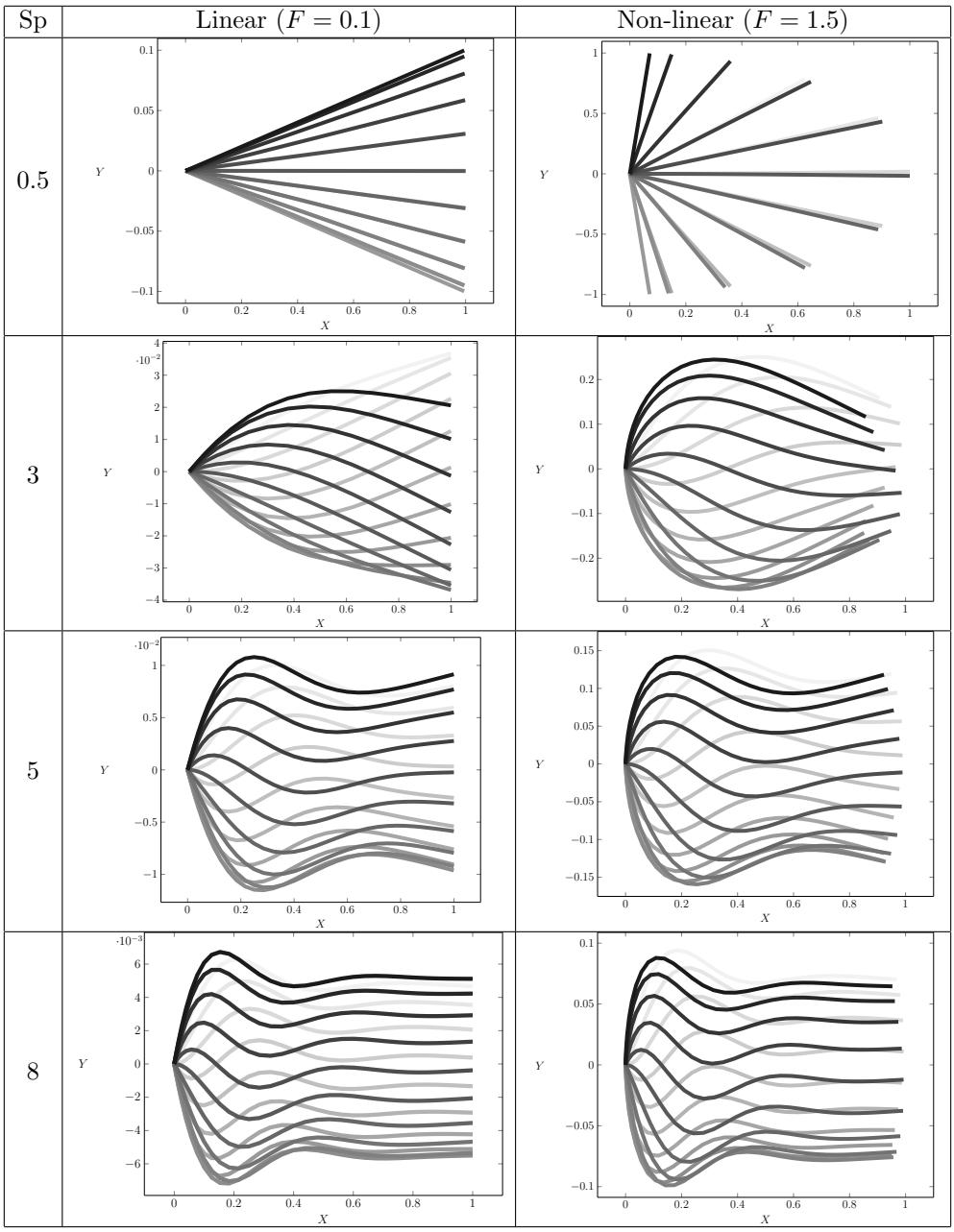

FIGURE 4. Filament shape in the filament-head reference frame. The shape is plotted over one full period where the shade of the filament indicates progression through the period, going from light to dark as time increases.

increase F beyond π, then we see the filament head moving in the direction of the tail for parts of its trajectory (which has effects on the swimming speed as we shall see). The biggest difference in shape seems to be for moderate values of Sp, values for which we expect to find a non-zero swimming speed.

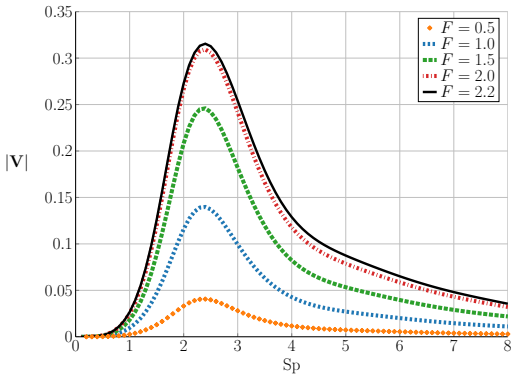

(A) Swimming speed as a function of the sperm-parameter Sp for different values of amplitude F.

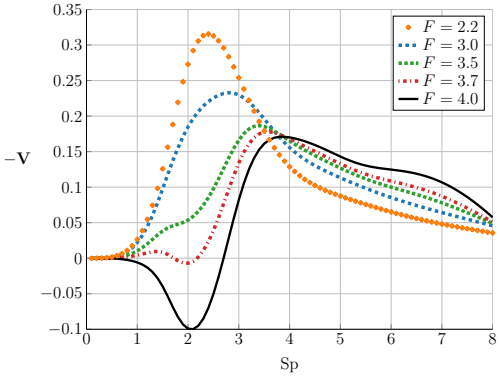

(B) Swimming speed as a function of the sperm-parameter Sp for high values of amplitude F.

FIGURE 5. Behaviour of the swimming speed as a function of Sp. For moderate values (up to $F \approx 2.2$) of F the profile for all values of F remains intact, see Figure 5a. For values higher than this we observe a dramatic change in profile, see Figure 5b.

Swimming speed. The main goal of the model is to describe a moving filament and therefore it is the swimming speed that is of final interest. The numerically found swimming speed is plotted as function of Sp in Figure 5. The swimming velocity vanishes for $\mathrm{Sp} \to 0$, which we anticipated in the previous section.

We observe furthermore in Figure 5a that there is a turning point in the curve, roughly for $\mathrm{Sp} \approx 2.4$, at which the swimming speed attains its maximum after which it decays again to zero confirming our preceding explanation and observations by Wiggins et al. [20] and Lauga [9].

Things are different when we increase the driving amplitude even further, from $F = 2.2$ to over $F = \pi$, thereby entering deeply into the non-linear regime. We observe that the profile that we found initially in Figure 5a changes, the shape peaks at $F \approx 2.2$ and for values higher the peak shifts in position towards higher Sp values and decreases in height, see Figure 5b. Moreover we observe a very peculiar reversal of sign of the swimming speed for certain ranges of Sp, if F is high enough. This implies a filament that swims in a reverse direction, from the head to the tail. A possible explanation of this goes back to the origin of the motion, namely the propulsive force. The direction of the velocity will point in the direction of the net propulsive force. Recall that the propulsive force was a result of the drag-anisotropy and depends on the direction of the filament and its velocity, see Figure 3. If the filament bends enough towards itself it can create the right geometry and velocity such that the contribution of propulsive forces in the tail direction start to increase and for certain values even dominate. Note however that one has to doubt the validity of the slender-body theory at this point, as it assumes a straight cylinder to find the hydrodynamic drag. If the filament is heavily bent, one might need to consider more refined drag models which could involve non-local filament-filament interactions, see for example [17].

Of course we want to compare the results from weakly non-linear analysis with the numerical realisations. Therefore we rescale the numeric swimming velocity by F^2 and look at the results for small F, see Figure 6a. We observe a perfect agreement between the analytic result and the numerical result, confirming a fixed profile for moderate values of F, only rescaled by F^2. Even for non-small values of F, $F = 0.5$ in this case, the agreement between numerics and analytics is

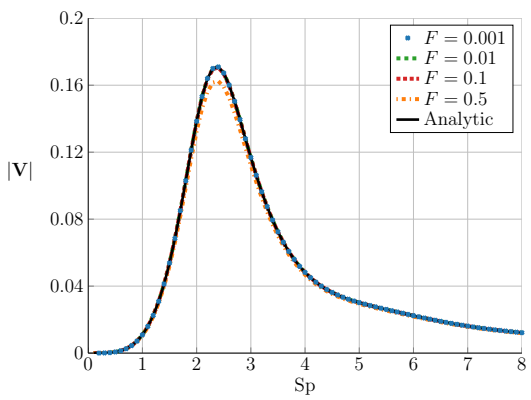

(A) Rescaled swimming speed as a function of the sperm-parameter Sp compared with analytic result.

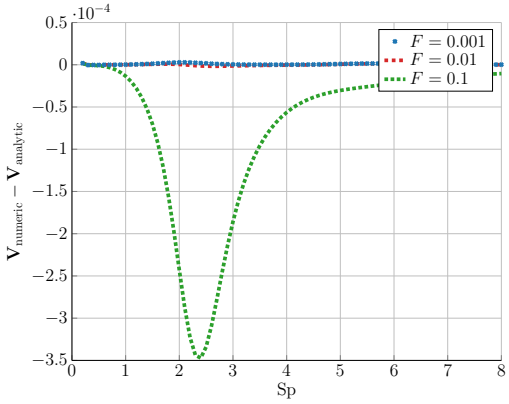

(B) Difference between the numeric swimming speed and the analytical result.

FIGURE 6. Behaviour of the swimming speed as a function of Sp rescaled by F^2 to compare with the (semi-)analytical result from Section 3. The difference between the analytics and numerics is shown in Figure 6b.

surprisingly close. The difference between the numerics and the analytics is depicted in Figure 6b. We observe that the difference is of the order $\mathcal{O}(F^4)$, which would mean that $\mathbf{V}^{(3)} = \mathbf{0}$. This can in fact be shown by taking the analysis from Section 3 one order further.

A last remark can be made in relation to the real value of Sp measured for human-spermatozoa, between 4 and 24. It appears that this value deviates substantially from the optimal value found for this model. However, one must note that the actual spermatozoa are active filaments, thus requiring an adaptation of the model.

5. Conclusion

We derived a model for a passive elastic filament in a viscous fluid driven by an external torque at the head. The resulting model gave a non-trivial propulsion of the filament, depending on an intricate interplay between bending forces and viscosity of the fluid, characterised by the sperm-parameter Sp. Results were found both analytically for small angles and numerically for a wide range of angles and were found to be consistent.

There are a few logical extensions to this work, mainly inspired by more careful analysis of biological micro-swimmers. Firstly, the inclusion of active elements along the filament creating an internal shear force could provide a better description of spermatozoa [2, 5]. In modelling sperm-cells one could look at the effects of a filament head on the dynamics [9]. As real biological movement takes place in three dimensions, allowing for corkscrew-like propulsion for example, it is interesting to see the effect of actuating the filament in three dimensions, see for example [9]. Observations hint that it is mainly high amplitude modulation of filaments in nature which propel organisms [10]. As mentioned this calls for a better understanding of the filament-filament interacting in the hydrodynamic drag formulation, hinting at improvements of the slender-body theory [17].

Acknowledgements

We would like to thank Dr. H. Gadêlha for useful discussions and guidance in the project. This work was carried out jointly with H. Mizuguchi, E. Parolin and V. Pereira.

Appendix A. Appendix

A.1. **Derivation elastic force.** To start out we need to rewrite our energy equation in terms of the filament geometry, described by $\mathbf{r}(s)$. To do so we use

$$\mathbf{r}_{ss} = \hat{\mathbf{t}}_s = \kappa \hat{\mathbf{n}}, \tag{47}$$

to express κ in terms of the position vector $\mathbf{r}$. Now the elastic energy takes the form

$$E[\mathbf{r}, \mathbf{r}_s, \mathbf{r}_{ss}] = \frac{1}{2}\int_0^L A(\mathbf{r}_{ss}\cdot\hat{\mathbf{n}})^2 + \Lambda|\mathbf{r}_s|^2 \,\mathrm{d}s. \tag{48}$$

Introduce a small deviation from the original shape, i.e. $\mathbf{r} + \delta\mathbf{r}$, and look at the resulting change in energy. Note that under this transformation we also get $\mathbf{r}_s + \delta\mathbf{r}_s$ and $\mathbf{r}_{ss} + \delta\mathbf{r}_{ss}$ and a change in unit vectors $\hat{\mathbf{n}} + \delta\hat{\mathbf{n}}$ (the change in $\hat{\mathbf{t}}$ is determined by the change in $\mathbf{r}_s$). This gives a changed energy

$$E[\mathbf{r}+\delta\mathbf{r}, \mathbf{r}_s+\delta\mathbf{r}_s, \mathbf{r}_{ss}+\delta\mathbf{r}_{ss}] = E[\mathbf{r}, \mathbf{r}_s, \mathbf{r}_{ss}] + \delta E + \mathcal{O}(\delta\mathbf{r}^2, \delta\mathbf{r}_s^2, \delta\mathbf{r}_{ss}^2), \tag{49}$$

where now the lowest order variation is given by

$$\delta E = \int_0^L A(\mathbf{r}_{ss}\cdot\hat{\mathbf{n}})(\mathbf{r}_{ss}\cdot\delta\hat{\mathbf{n}} + \delta\mathbf{r}_{ss}\cdot\hat{\mathbf{n}}) + \Lambda\mathbf{r}_s\cdot\delta\mathbf{r}_s \,\mathrm{d}s \tag{50}$$

$$= \int_0^L A\kappa(\kappa\hat{\mathbf{n}}\cdot\delta\hat{\mathbf{n}} + \delta\mathbf{r}_{ss}\cdot\hat{\mathbf{n}}) + \Lambda\hat{\mathbf{t}}\cdot\delta\mathbf{r}_s \,\mathrm{d}s \tag{51}$$

$$= \int_0^L A\kappa\hat{\mathbf{n}}\cdot\delta\mathbf{r}_{ss} + \Lambda\hat{\mathbf{t}}\cdot\delta\mathbf{r}_s \,\mathrm{d}s, \tag{52}$$

where in the last step we used that $\hat{\mathbf{n}}\cdot\delta\hat{\mathbf{n}} = 0$. This must be true in order to ensure that the unit vectors stay normalized under the variation. Using integration by parts this variational energy can be rewritten as

$$\delta E = \int_0^L A\kappa\hat{\mathbf{n}}\cdot\delta\mathbf{r}_{ss} + \Lambda\hat{\mathbf{t}}\cdot\delta\mathbf{r}_s \,\mathrm{d}s \tag{53}$$

$$= \left[A\kappa\hat{\mathbf{n}}\cdot\delta\mathbf{r}_s + \Lambda\hat{\mathbf{t}}\cdot\delta\mathbf{r}\right]_0^L - \int_0^L A(\kappa\hat{\mathbf{n}})_s\cdot\delta\mathbf{r}_s + (\Lambda\hat{\mathbf{t}})_s\cdot\delta\mathbf{r}\,\mathrm{d}s \tag{54}$$

$$= \left[A\kappa\hat{\mathbf{n}}\cdot\delta\mathbf{r}_s + (\Lambda\hat{\mathbf{t}} - A(\kappa\hat{\mathbf{n}})_s)\cdot\delta\mathbf{r}\right]_0^L + \int_0^L A(\kappa\hat{\mathbf{n}})_{ss}\cdot\delta\mathbf{r} - (\Lambda\hat{\mathbf{t}})_s\cdot\delta\mathbf{r}\,\mathrm{d}s \tag{55}$$

$$= \left[A\kappa\hat{\mathbf{n}}\cdot\delta\mathbf{r}_s + (-A\kappa_s\hat{\mathbf{n}} + (\Lambda + A\kappa^2)\hat{\mathbf{t}})\cdot\delta\mathbf{r}\right]_0^L + \int_0^L (A\kappa_s\hat{\mathbf{n}} - (A\kappa^2+\Lambda)\hat{\mathbf{t}})_s\cdot\delta\mathbf{r}\,\mathrm{d}s \tag{56}$$

$$= \left[A\kappa\hat{\mathbf{n}}\cdot\delta\mathbf{r}_s + (-A\kappa_s\hat{\mathbf{n}} + \tau\hat{\mathbf{t}})\cdot\delta\mathbf{r}\right]_0^L + \int_0^L \partial_s\left[A\kappa_s\hat{\mathbf{n}} - \tau\hat{\mathbf{t}}\right]\cdot\delta\mathbf{r}\,\mathrm{d}s. \tag{57}$$

So we retrieve (12) and by neglecting the quadratic and higher order contributions the elastic force and boundary conditions can be derived from this expression giving the state of minimal elastic energy.

A.2. **Slender-body theory.** The main motivation for the slender-body theory is the linearity of the Stokes equation (3), which opens the door to the principle of superposition in constructing solutions. By starting from the solutions of a point-source problem, called Stokeslet,

$$-\mathbf{F}\delta(\mathbf{r}) = -\nabla p + \nabla^2 \mathbf{u}, \qquad \nabla \cdot \mathbf{u} = 0, \tag{58}$$

we construct an (approximate) solution to the problem of flow around a finite length cylinder. To construct a solution we follow [21], first use the fact that $\mathbf{u}$ is divergence-less to get

$$\nabla \cdot (\mathbf{F}\delta(\mathbf{r})) = \nabla^2 p. \tag{59}$$

Then apply a Fourier-transform to this equation to get

$$i\mathbf{k} \cdot \mathbf{F} = k^2 \hat{p}, \tag{60}$$

where now $\hat{}$ depicts the Fourier-transformed function and therefore

$$\hat{p} = \frac{i\mathbf{k} \cdot \mathbf{F}}{k^2}. \tag{61}$$

Using this we can transform (58) and find an expression for $\hat{\mathbf{u}}$

$$\hat{\mathbf{u}} = \frac{1}{k^2}\left(\mathbf{F} - \frac{\mathbf{k}\mathbf{k} \cdot \mathbf{F}}{k^2}\right) = \frac{1}{k^2}\left(\mathbb{1} - \frac{\mathbf{k}\mathbf{k}}{k^2}\right) \cdot \mathbf{F}. \tag{62}$$

The Fourier transforms of the fundamental solution to Laplace and biharmonic equations then give that

$$\mathcal{F}^{-1}\left(\frac{i\mathbf{k}}{k^2}\right) = -\nabla\left(\frac{1}{4\pi r}\right) = \frac{\mathbf{r}}{4\pi r^3}, \tag{63}$$

$$\mathcal{F}^{-1}\left(\frac{\mathbb{1}}{k^2}\right) = \left(\frac{\mathbb{1}}{4\pi r}\right), \tag{64}$$

$$\mathcal{F}^{-1}\left(\frac{\mathbf{k}\mathbf{k}}{k^4}\right) = \nabla\nabla\left(\frac{r}{8\pi}\right) = \frac{1}{8\pi}\nabla\left(\frac{\mathbf{r}}{r}\right) = \frac{1}{8\pi}\left(\frac{\mathbb{1}}{r} - \frac{\mathbf{r}\mathbf{r}}{r^3}\right). \tag{65}$$

(66)

From this we can distil that

$$p = \frac{\mathbf{F} \cdot \mathbf{r}}{4\pi r^3}, \tag{67}$$

$$\mathbf{u} = \frac{1}{8\pi}\left(\frac{\mathbb{1}}{r} + \frac{\mathbf{r}\mathbf{r}}{r^3}\right) \cdot \mathbf{F}, \tag{68}$$

which is the Stokeslet solution. In order to construct our approximation we also need to consider other singularity solutions to the Stokes equations. The one directly needed are a special class of solutions, often called source singularities, with

$$\mathbf{0} = \nabla^2 \mathbf{u}, \quad \nabla \cdot \mathbf{u} = 0, \quad p = 0, \tag{69}$$

which we can cast into flow potential form if we use $\mathbf{u} = \nabla\phi$, with a harmonic potential ϕ. If we pick a classical dipole potential (like in electrostatics theory and in fact very similar to (67)), i.e.

$$\phi = \frac{\mathbf{G} \cdot \mathbf{r}}{4\pi r^3}, \tag{70}$$

then the derived velocity $\mathbf{u}$ satisfies (69) and is called a source doublet. If we carefully take the gradient of this potential (see for example [6]) we find

$$\mathbf{u} = \frac{1}{4\pi}\left(\frac{\mathbb{1}}{r^3} - \frac{3\mathbf{r}\mathbf{r}}{r^5}\right) \cdot \mathbf{G} + \frac{1}{3}\delta(\mathbf{r})\mathbf{G}. \tag{71}$$

With these Stokeslet and source-doublet solutions we now construct an approximate solution.

To do so we consider a cylinder of length L and radius a. We look at the result that a distribution of Stokeslets and doublets along the centreline of the cylinder has on the edge of the cylinder. Note that we need to assume a slender cylinder, so $\frac{a}{L} \ll 1$. Choose the axis system such that the $\hat{\mathbf{z}}$ axis aligns with the long axis of the cylinder and the origin to lie on the centreline, although not necessarily at the centre of it. As we already use $\mathbf{r}$ for position, we introduce $\hat{\mathbf{n}}$ as the unit radial vector, in accordance with the notation of the one-dimensional filament, the remaining unit vector for the angle is denoted by $\hat{\boldsymbol{\theta}}$. We consider the effect of the distribution on the circular cross-section at $z = 0$ by integrating the effect of the sources on the centreline[2]. We consider two cases, $\mathbf{F} = f\hat{\mathbf{z}}$, tangential Stokeslets ($\hat{\mathbf{t}}$ direction in the one-dimensional case), and $\mathbf{F} = f\hat{\mathbf{n}}$, normal or radial Stokeslets.
Now any point on the edge of the cylinder can be described by $\mathbf{r} = a\hat{\mathbf{n}} + z\hat{\mathbf{z}} + \theta\hat{\boldsymbol{\theta}}$. If we define b and c the distance from the origin to the ends of the filament then we are interested in

$$\bar{\mathbf{u}}(a,\theta) = \int_{-b}^{c} \mathbf{u}(a,z,\theta)\,\mathrm{d}z. \tag{72}$$

In order to calculate these integrals we use that $r^2 = z^2 + a^2$, the distance from the Stokeslets to the cross-section. Furthermore we use the following integrals

$$\int_{-b}^{c} \frac{1}{r^3}\,\mathrm{d}z \approx \int_{-\infty}^{\infty} \frac{1}{r^3}\,\mathrm{d}z = \int_{-\infty}^{\infty} \frac{1}{(z^2+a^2)^{\frac{3}{2}}}\,\mathrm{d}z = \frac{2}{a^2}, \tag{73}$$

$$\int_{-b}^{c} \frac{z}{r^3}\,\mathrm{d}z \approx \int_{-\infty}^{\infty} \frac{z}{r^3}\,\mathrm{d}z = \int_{-\infty}^{\infty} \frac{z}{(z^2+a^2)^{\frac{3}{2}}}\,\mathrm{d}z = 0, \tag{74}$$

$$\int_{-b}^{c} \frac{1}{r^5}\,\mathrm{d}z \approx \int_{-\infty}^{\infty} \frac{1}{r^5}\,\mathrm{d}z = \int_{-\infty}^{\infty} \frac{1}{(z^2+a^2)^{\frac{5}{2}}}\,\mathrm{d}z = \frac{4}{3a^4}, \tag{75}$$

$$\int_{-b}^{c} \frac{z}{r^5}\,\mathrm{d}z \approx \int_{-\infty}^{\infty} \frac{z}{r^5}\,\mathrm{d}z = \int_{-\infty}^{\infty} \frac{z}{(z^2+a^2)^{\frac{5}{2}}}\,\mathrm{d}z = 0, \tag{76}$$

where we use the fact that b, c are large compared to a. For integrands that decay like $\frac{1}{r}$ we can't use this procedure as the integrals won't converge. Instead we use a different approximation of the exact integral

$$\int_{-b}^{c} \frac{1}{r}\,\mathrm{d}z = \int_{-b}^{c} \frac{1}{(z^2+a^2)^{\frac{1}{2}}}\,\mathrm{d}z = \log\left[\left(c+\sqrt{c^2+a^2}\right)\left(-b+\sqrt{b^2+a^2}\right)^{-1}\right] \tag{77}$$

$$= \log\left[\frac{1}{a^2}\left(c+\sqrt{c^2+a^2}\right)\left(b+\sqrt{b^2+a^2}\right)\right] \tag{78}$$

$$= \log\left[\left(\frac{c}{a}+\sqrt{\left(\frac{c}{a}\right)^2+1}\right)\left(\frac{b}{a}+\sqrt{\left(\frac{b}{a}\right)^2+1}\right)\right] \tag{79}$$

$$\approx \log\left[4\frac{cb}{a^2}\right], \tag{80}$$

[2]Note that this allows us to look at any cross-section as we haven't fixed the origin position.

and

$$\int_{-b}^{c} \frac{z^2}{r^3}\,\mathrm{d}z = \int_{-b}^{c} \frac{z^2}{(z^2+a^2)^{\frac{3}{2}}}\,\mathrm{d}z \tag{81}$$

$$= \log\left[\left(c+\sqrt{c^2+a^2}\right)\left(-b+\sqrt{b^2+a^2}\right)^{-1}\right] - \frac{c}{\sqrt{c^2+a^2}} - \frac{b}{\sqrt{b^2+a^2}} \tag{82}$$

$$= \log\left[\left(c+\sqrt{c^2+a^2}\right)\left(-b+\sqrt{b^2+a^2}\right)^{-1}\right] - \frac{1}{\sqrt{1+\left(\frac{a}{c}\right)^2}} - \frac{1}{\sqrt{1+\left(\frac{a}{b}\right)^2}} \tag{83}$$

$$\approx \log\left[4\frac{cb}{a^2}\right] - 2. \tag{84}$$

Using these integrals we find in the case of normal Stokeslets, i.e. $\mathbf{F} = f\hat{\mathbf{n}}$, that the Stokeslet contribution is given by

$$\bar{\mathbf{u}}_{\text{Stokeslet}}(a,\theta) = \frac{f}{8\pi}\int_{-b}^{c}\left(\frac{\mathbb{1}}{r}+\frac{\mathbf{rr}}{r^3}\right)\cdot\hat{\mathbf{n}}\,\mathrm{d}z \approx \frac{f}{8\pi}\left[\left(\log\left(4\frac{cb}{a^2}\right)+2\right)\hat{\mathbf{n}} + 2\frac{\theta}{a}\hat{\boldsymbol{\theta}}\right]. \tag{85}$$

Note that this depends on θ, something which is not physical on symmetry considerations. Therefore we need to add source-doublets to cancel the contributions in the $\hat{\boldsymbol{\theta}}$ direction. If we put in a distribution of source-doublets pointing in the same direction of strength g, i.e. $\mathbf{G} = g\hat{\mathbf{n}}$, we find

$$\bar{\mathbf{u}}_{\text{Doublet}}(a,\theta) = \frac{g}{4\pi}\int_{-b}^{c}\left(\frac{\mathbb{1}}{r^3}-\frac{3\mathbf{rr}}{r^5}\right)\cdot\hat{\mathbf{n}}\,\mathrm{d}z \approx \frac{g}{4\pi}\left[-\frac{2}{a^2}\hat{\mathbf{n}} - \frac{4\theta}{a^3}\hat{\boldsymbol{\theta}}\right]. \tag{86}$$

Thus we see that if $g = \frac{fa^2}{4}$ we get a combined contribution of Stokeslets and source-doublets which give on the edge of the cylinder

$$\bar{\mathbf{u}}(a,\theta) \approx \frac{f}{8\pi}\left(\log\left(4\frac{cb}{a^2}\right)+1\right)\hat{\mathbf{n}}. \tag{87}$$

Now for the case of tangential Stokeslets the analysis is slightly easier as

$$\begin{aligned}\bar{\mathbf{u}}_{\text{Stokeslet}}(a,\theta) &= \frac{f}{8\pi}\int_{-b}^{c}\left(\frac{\mathbb{1}}{r}+\frac{\mathbf{rr}}{r^3}\right)\cdot\hat{\mathbf{z}}\,\mathrm{d}z \approx \frac{f}{8\pi}\left(\log\left(4\frac{cb}{a^2}\right)+\log\left[4\frac{cb}{a^2}\right]-2\right)\hat{\mathbf{z}}\\ &= \frac{f}{4\pi}\left(\log\left(4\frac{cb}{a^2}\right)-1\right)\hat{\mathbf{z}}.\end{aligned} \tag{88}$$

Therefore we do not need to add source-doublets as the result from Stokeslets only is already a unidirectional velocity profile.

If we now translate these results to the one-dimensional filament under consideration in this paper, we find that

$$\mathbf{f}_{\mathcal{H}} = -\xi_{\parallel}\mathbf{u}_{\parallel} - \xi_{\perp}\mathbf{u}_{\perp}, \tag{89}$$

were

$$\xi_{\perp} \approx \frac{8\pi}{\log\left(4\frac{cb}{a^2}\right)+1}, \qquad \xi_{\parallel} \approx \frac{4\pi}{\log\left(4\frac{cb}{a^2}\right)-1}. \tag{90}$$

Therefore we see that there is indeed anisotropy, depending on the slenderness of the filament, captured by $\frac{cb}{a^2}$,

$$\beta = \frac{1}{2}\left(\frac{\log\left(4\frac{cb}{a^2}\right)+1}{\log\left(4\frac{cb}{a^2}\right)-1}\right). \tag{91}$$

In the limit of exponentially slender filaments, i.e. $\log\left(\frac{cb}{a^2}\right) \gg 1$, we see that $\beta \to \frac{1}{2}$. Note however that for more moderate values of the slenderness $\beta > \frac{1}{2}$, which is discussed by [11]. A

more accurate treatment can justify the use of these straight cylinder approximation in the case of a periodically driven filament, thus incorporating bending of the filament, see [11].

A.3. **IMEX-schemes.** The result of the spatial discretisation of (22) is a system of ODEs for the spatial discretisation $\mathbf{\Psi}$ of ψ and algebraic equations for the spatial discretisation $\mathbf{T}$ of τ depicted by

$$\begin{cases} \frac{d}{dt}\mathbf{\Psi}(t) &= \mathbf{F}_1(t,\mathbf{\Psi}(t)) + \mathbf{F}_2(t,\mathbf{\Psi}(t),\mathbf{T}(t)), \\ D\mathbf{T}(t) &= \mathbf{F}_3(t,\mathbf{\Psi}(t))\mathbf{T}(t) + \mathbf{F}_4(t,\mathbf{\Psi}(t)). \end{cases} \tag{92}$$

Here we choose to take $\mathbf{F}_1$ to depict the hyperdiffusion part, i.e. ψ_{ssss}, and $\mathbf{F}_2$ the non-linear terms and coupling between ψ, τ. Furthermore $\mathbf{F}_3 = \mathrm{diag}(\mathbf{\Psi}(t))$ and $\mathbf{F}_4$ depicts the non-linear contributions of ψ to the τ equation.
We then step in time using equispaced timesteps Δt. A choice must be made whether to employ explicit or implicit integration in time of the system of ODEs. As the factor $\mathbf{F}_1$ is usually stiff, recall results for diffusion, we would need a severe restriction on the timestep Δt in order for a stable explicit integration in time. On the other hand, an implicit integration would leave us with no other option than to use Newton-iterations every time-step which would put a heavy strain on the computational time. In order to circumvent this we employ an IMEX scheme, i.e. treating the stiff parts implicitly and the remaining terms explicitly. Two methods considered are the first-order scheme IMEX-Euler and the second order scheme IMEX-2BDF [8]

$$\begin{aligned} \frac{3}{2}\mathbf{\Psi}^{n+1} - 2\mathbf{\Psi}^n + \frac{1}{2}\mathbf{\Psi}^{n-1} &= \Delta t\mathbf{F}_1^{n+1} + \Delta t\left(2\mathbf{F}_2^n - \mathbf{F}_2^{n-1}\right) && \textit{IMEX-2BDF}, \\ \mathbf{\Psi}^{n+1} - \mathbf{\Psi}^n &= \Delta t\mathbf{F}_1^{n+1} + \Delta t\mathbf{F}_2^n && \textit{IMEX-Euler}, \end{aligned}$$

where $\mathbf{F}_1^n = \mathbf{F}_1(t_n, \mathbf{\Psi}^n), \mathbf{F}_2^n = \mathbf{F}_2(t_n, \mathbf{\Psi}^n, \mathbf{T}^n)$. Note furthermore that $\mathbf{F}_1$ is a linear function of $\mathbf{\Psi}$ and the result is thus a solvable matrix equation for $\mathbf{\Psi}^{n+1}$.
After calculation of $\mathbf{\Psi}^{n+1}$ we can solve for the tension $\mathbf{T}^{n+1}$ by using

$$(D - \mathbf{F}_3^{n+1})\mathbf{T}^{n+1} = \mathbf{F}_4^{n+1}. \tag{93}$$

The scheme used for the simulations in the paper is IMEX-2BDF as the IMEX-2BDF scheme is second order in time, thus achieving higher accuracy in time-stepping. Furthermore, the computational extra time needed compared to IMEX-Euler appears to be negligible if implemented correctly.

The convergence results for both schemes were tested using the method of manufactured solutions [14]. In short, we want to test convergence by comparing simulations to analytical solutions. These exact solutions are not available for our problem, and many other non-linear problems. For a general equation

$$L(\mathbf{X}) = \mathbf{0}, \tag{94}$$

where $\mathbf{X} = (\psi, \tau)^T$ in our case, we can change the problem slightly by adding a source term so that we know the exact solution. If we pick any function $\tilde{\mathbf{X}}$ satisfying the boundary conditions for ψ, τ, then we note that in general $L(\tilde{\mathbf{X}}) \neq \mathbf{0}$. It does however provide us with an exact solution to the problem

$$L(\mathbf{X}) = \mathbf{F}, \tag{95}$$

where $\mathbf{F} = L(\tilde{\mathbf{X}})$ is now a source term, the solution is in that case of course $\tilde{\mathbf{X}}$. So we numerically solve the system $L(\mathbf{X}) - \mathbf{F} = \mathbf{0}$ instead of the original system. That way we can compare the numerical results with an analytical solution $\tilde{\mathbf{X}}$ to find the convergence rates of the schemes.
By choosing $\tau \equiv 0$ and $\psi(s,t) = F\cos(2\pi t)(1 - s^4 + 2s^3 - 2s)$, so that all the boundary conditions are satisfied, we find perfect agreement with theory of the IMEX-schemes [1]. The IMEX-2BDF

scheme is of second order and the Euler method is of first order, see Figure 7. This justifies the choice of the IMEX-2BDF scheme in the simulations.

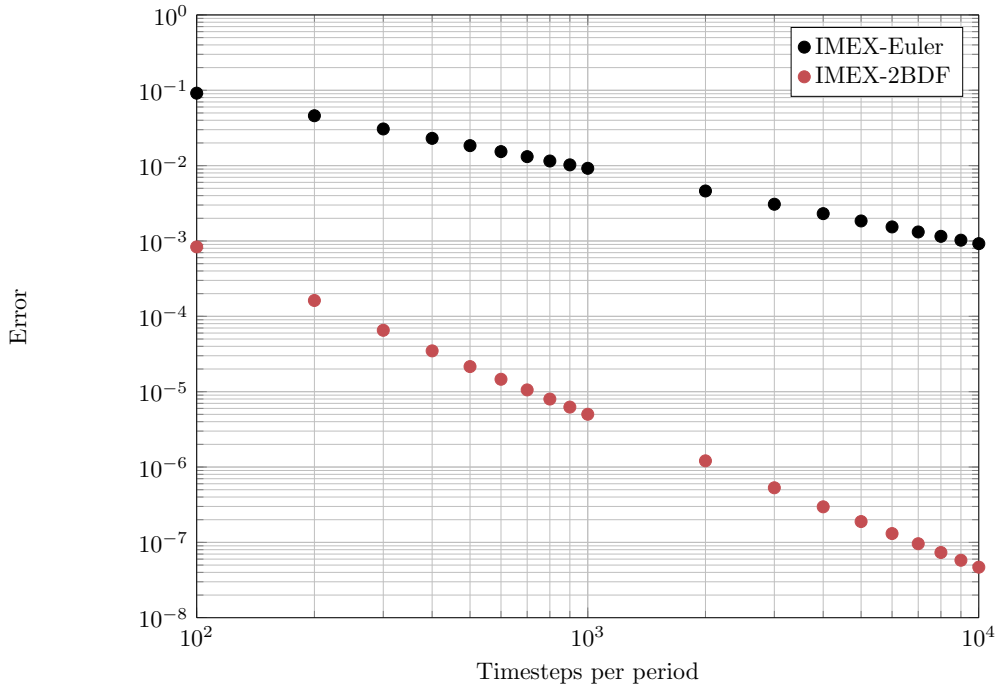

FIGURE 7. Convergence loglog-plot for both of the IMEX-schemes constructed using the method of manufactured solutions. The slope of the straight line for the Euler method is one, indicating first order convergence in time. The slope of the IMEX-2BDF scheme indicates its second order convergence in time.

References

1. Ascher, U. M., Ruuth, S. J. & Wetton, B. T. R. Implicit-Explicit Methods for Time-Dependent Partial Differential Equations. *SIAM Journal on Numerical Analysis* **32,** 797–823 (1995).
2. Camalet, S. & Jülicher, F. Generic aspects of axonemal beating. *New Journal of Physics* **2,** 24–24 (2000).
3. Darnton, N. C., Turner, L., Rojevsky, S. & Berg, H. C. On torque and tumbling in swimming Escherichia coli. *Journal of bacteriology* **189,** 1756–64 (2007).
4. Dyke, M. V. *Perturbation Methods in Fluid Mechanics* (Parabolic Press, 1975).
5. Gadêlha, H, Gaffney, E. A., Smith, D. J. & Kirkman-Brown, J. C. Nonlinear instability in flagellar dynamics: a novel modulation mechanism in sperm migration? *Journal of the Royal Society, Interface / the Royal Society* **7,** 1689–97 (2010).
6. Griffiths, D. J. Hyperfine splitting in the ground state of hydrogen. *American Journal of Physics* **50,** 698 (1982).
7. Hancock, G. J. The Self-Propulsion of Microscopic Organisms through Liquids. *Proceedings of the Royal Society A: Mathematical, Physical and Engineering Sciences* **217,** 96–121 (1953).
8. Hundsdorfer, W. & Verwer, J. G. *Numerical Solution of Time-Dependent Advection-Diffusion-Reaction Equations* (Springer Science & Business Media, 2003).
9. Lauga, E. Floppy swimming: Viscous locomotion of actuated elastica. *Physical Review E* **75,** 041916 (2007).
10. Lauga, E. & Powers, T. R. The hydrodynamics of swimming microorganisms. *Reports on Progress in Physics* **72** (2009).
11. Lighthill, J. *Mathematical Biofluiddynamics* (Society for Industrial and Applied Mathematics, 1975).
12. Marquez, B. & Suarez, S. S. Different signaling pathways in bovine sperm regulate capacitation and hyperactivation. *Biology of reproduction* **70,** 1626–33 (2004).
13. Purcell, E. M. Life at low Reynolds number. *American Journal of Physics* **45** (1977).
14. Roache, P. J. Code Verification by the Method of Manufactured Solutions. *Journal of Fluids Engineering* **124,** 4 (2002).
15. Rohr, J, Latz, M. I., Fallon, S, Nauen, J. C. & Hendricks, E. Experimental approaches towards interpreting dolphin-stimulated bioluminescence. *J. Exp. Biol.* **201,** 1447–1460 (1998).
16. Taylor, G. Analysis of the Swimming of Microscopic Organisms. *Proceedings of the Royal Society A: Mathematical, Physical and Engineering Sciences* **209,** 447–461 (1951).
17. Tornberg, A.-K. & Shelley, M. J. Simulating the dynamics and interactions of flexible fibers in Stokes flows. *Journal of Computational Physics* **196,** 8–40 (2004).
18. Trefethen, L. N. *Spectral Methods in MATLAB* (Society for Industrial and Applied Mathematics, 2000).
19. Wiggins, C. H., Riveline, D, Ott, A & Goldstein, R. E. Trapping and wiggling: elastohydrodynamics of driven microfilaments. *Biophysical journal* **74,** 1043–60 (1998).
20. Wiggins, C. & Goldstein, R. Flexive and Propulsive Dynamics of Elastica at Low Reynolds Number. *Physical Review Letters* **80,** 3879–3882 (1998).
21. Zapryanov, Z. & Tabakova, S. *Dynamics of Bubbles, Drops and Rigid Particles* (Springer Netherlands, Dordrecht, 1999).